Fragment-mass distributions in neutron-induced fission of ^{232}Th and ^{238}U at 33, 45, and 60 MeV

I. V. Ryzhov, S. G. Yavshits, G. A. Tutin, N. V. Kovalev, A. V. Saulski, and N. A. Kudryashev
V. G. Khlopin Radium Institute, Second Murinskiy prospect 28, 194021, Saint Petersburg, Russia

M. S. Onegin, L. A. Vaishnene, and Yu. A. Gavrikov
Petersburg Nuclear Physics Insitute, 188300, Gatchina, Leningrad district, Russia

O. T. Grudzevich
State Technical University, Studgorodok 1, 249020, Kaluga region, Obninsk, Russia

V. D. Simutkin,* S. Pomp, J. Blomgren, M. Österlund, P. Andersson, and R. Bevilacqua
Department of Physics and Astronomy, Uppsala University, Box 516, SE-751 20 Uppsala, Sweden

J. P. Meulders and R. Prieels
Institute of Nuclear Physics, Université Catholique de Louvain, B-1348 Louvain-la Neuve, Belgium
(Received 22 November 2010; published 6 May 2011)

We have measured fission fragment-mass yields for neutron-induced fission of ^{232}Th and ^{238}U at energies 32.8, 45.3, and 59.9 MeV. The experiments were done at quasimonoenergetic neutron beams of the Cyclotron Research Center at Louvain-la-Neuve. To detect the fission fragments, a multisection Frisch-gridded ionization chamber was used. The measurement and data analysis techniques are discussed in detail. The obtained mass yields are compared to model calculations with the intermediate-energy nuclear reaction code MCFX. The MCFX code is used to calculate the fraction of fissioning nuclei after cascade, preequilibrium, and statistical reaction stages. The formation of mass distributions is considered as a result of oscillations of the mass-asymmetry degree of freedom in the potential well calculated with the temperature-dependent shell correction method. The experimental results as well as the results of the model calculations demonstrate that the probability of symmetric fission increases with incident neutron energy for both nuclei. The comparison also shows that the symmetric fission is more enhanced for thorium than for uranium with increasing neutron energy. We also compare ^{238}U results with available experimental data; the ^{232}Th data were measured for the first time.

DOI: 10.1103/PhysRevC.83.054603 PACS number(s): 25.85.Ec, 25.40.−h, 27.90.+b

I. INTRODUCTION

The history of fission research started over 70 years ago with the discovery of neutron-induced fission of uranium [1]. From that time onward neutron-induced fission of actinides has been the subject of both fundamental and applied studies. In the past, tremendous effort has been put into studies of low-energy actinide fission because of the particular importance of this process for nuclear energy applications. Nowadays, there is an increasing interest in studying neutron-induced fission of actinides at intermediate energies, i.e., between 20 and 200 MeV. It is motivated by nuclear data needs for feasibility studies of emerging nuclear systems dedicated to the generation of intense radioactive ion beams, incineration of nuclear waste, isotope production, etc. Nevertheless, after many years of research, neutron-induced fission of actinides remains an intriguing subject of studies in nuclear physics and astrophysics (in the latter case the fission process is considered as an important part of the *r*-process nucleosynthesis [2]).

The fragment-mass distribution is one of the most important characteristics of the nuclear fission process. At present a consistent description of mass splitting in fission is far from being achieved. It is believed that the formation of the fission fragment-mass distribution is closely connected with the potential energy surface in deformation space (at the stage of saddle-to-scission descent) while dynamical effects (nuclear friction and inertia) have less influence on the shape of the mass spectra. A number of theoretical models have been proposed at different times to quantitatively predict fragment-mass yields [3–7]. It should be pointed out that modeling of intermediate-energy neutron-induced fission is severely complicated by the fact that fission, being a relatively slow process, follows preequilibrium particle emission and competes with neutron evaporation. As a result, a number of nuclides, each with its own fission characteristics, will contribute to the experimental fission observables. This suggests that a model of fragment formation should be embedded in a proper nuclear reaction code which takes care of prefission particle emission (see, e.g., [8,9]).

Further development of the fission reaction models requires new experimental data at intermediate energies. To date the neutron-induced fission cross sections of many actinides relevant to advanced nuclear applications have been measured at incident energies up to 200 MeV [10–13], but there is a lack of experimental data on fragment-mass yields. The only

*Corresponding author; vasily.simutkin@fysast.uu.se

data have been obtained at the white neutron beam of the Los Alamos Neutron Science Center (LANSCE), where the mass yields have been measured in neutron-induced fission of ^{238}U at energies up to 500 MeV [14]. In this work we report on measurements of fragment-mass yields in fission of ^{238}U and ^{232}Th by quasimonoenergetic neutrons with energies from 30 to 60 MeV. The measurement techniques and data analysis are described in detail in Secs. II and III, respectively. Section IV contains the measurement results in comparison with data obtained at LANSCE. Model calculations based on the intermediate energy nuclear reaction code MCFX [9] are considered in Sec. V. Discussion of the results and conclusions are given in Secs. VI and VII, respectively.

II. MEASUREMENTS

A. Experimental arrangement

The experiment was carried out at the neutron beam of the cyclotron facility CYCLONE in Louvain-la-Neuve (LLN). The facility has been described in detail in Refs. [15,16], and therefore only a brief description is given below. The experimental arrangement is shown in Fig. 1. Quasimonoenergetic neutrons are produced by the ^{7}Li(p,n) reaction. Protons delivered by the cyclotron pass through a carbon collimator and impinge on a 5-mm-thick water-cooled natural lithium target with a diameter of 7 mm. Neutrons enter the experimental area while the primary beam is bent to a water-cooled carbon dump. An iron collimator defines the neutron beam with a diameter of about 2 cm at a distance of 2 m from the Li target.

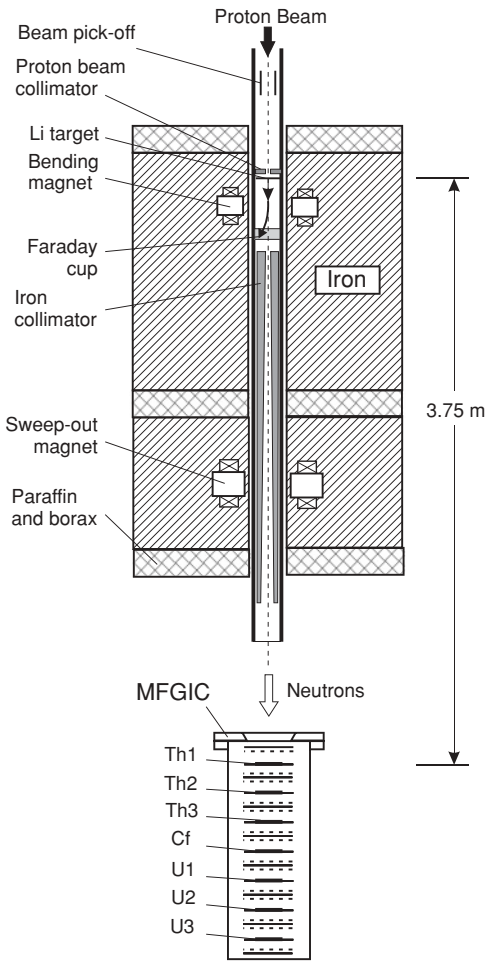

FIG. 1. General layout (not to scale) of the measurements at the LLN neutron beam facility.

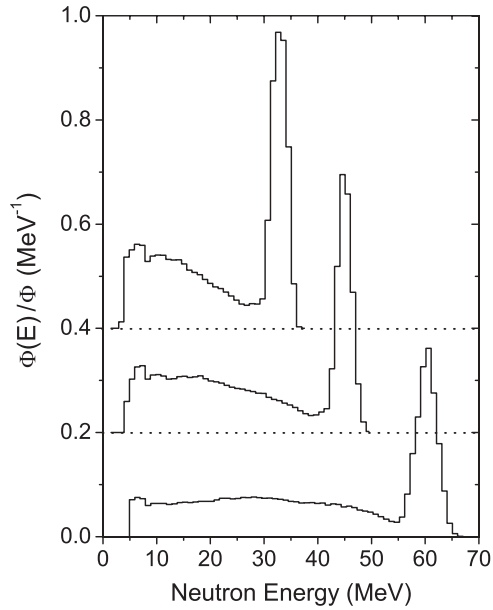

FIG. 2. Relative spectral fluence of the quasimonoenergetic neutron beams produced with the ^{7}Li(p,n) reaction at the LLN neutron beam facility [17]. The spectra were obtained at 0° with respect to the proton beam axis; the target thickness was 5 mm. The gap at lower energies is caused by the registration threshold of the detector used in Ref. [17]. The spectra are offset along the y axis for better visualization.

In this work, proton beams with energies of 36.4, 48.5, and 62.9 MeV were used. The neutron spectra produced at an angle of 0° with respect to the proton beam axis are given in Fig. 2 [17]. One can see that a typical neutron spectrum consists of a well-defined peak followed by a continuum of lower-energy neutrons. The high-energy peak contains 30%–40% of all neutrons and has a full width at half maximum of a few MeV depending on the incident proton energy and the thickness of the lithium target. The corresponding neutron peak energies, 32.8, 45.3, and 59.9 MeV, were calculated from the incident proton energy, the Q value of the ^{7}Li(p,n) reaction, and the energy loss of the protons in the target.

The first fissile target was located at a distance of 375 cm from the Li target. The distance between the targets was 6.4 cm. At the target positions, the fluence rate of the peak neutrons was about 10^{5} cm^{-2} s^{-1}.

B. Fission fragment detector

A multisection Frisch-gridded ionization chamber (MFGIC) similar to that described in Ref. [18] was used to detect fission fragments. A schematic view of the MFGIC electrode assembly is shown at the top of Fig. 3. The detector

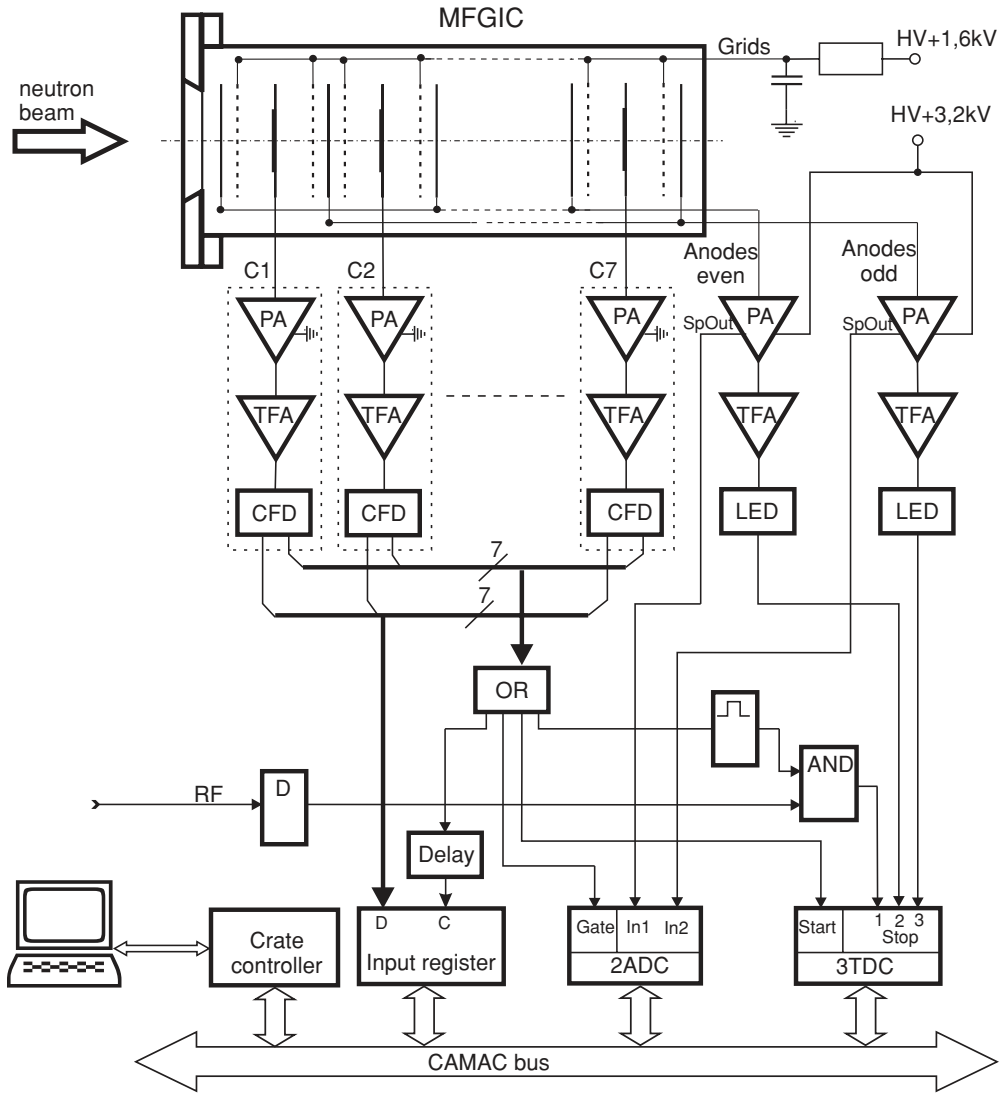

FIG. 3. Block diagram of the electronic layout used for measurements with the MFGIC.

consists of seven sections. Each section constitutes a twin Frisch-gridded ionization chamber with a common cathode. Adjacent sections have a common anode, so the total number of the electrodes is 29 including 7 cathodes, 8 anodes, and 14 grids. The electrode assembly is placed into a thin-walled (1 mm) stainless steel detector housing. All the electrodes are of circular form with a diameter of 110 mm. The anodes are Duralumin foils, 50 μm thick, sandwiched between two 1-mm-thick Duralumin rings with inner diameter of 90 mm. The cathodes are stainless steel annular disks of 2 mm thick and 68 mm inner diameter. The target holders are mounted in the central part of each cathode using spring catches. The grids are mounted in parallel on stainless steel rings that are 2 mm thick and have 90 mm inner diameter. The grids are made of gilded molybdenum wires of 80 μm in diameter spaced by 1.25 mm. The distance between anode and grid is 8 mm. The cathode to grid distance is 24 mm. The working gas mixture is composed of 90% argon and 10% methane (P-10). The chamber operates at pressure of 1.16 bar (without a continuous gas flow).

C. Targets

The fissile targets were prepared by vacuum evaporation of $^{nat}UF_4$ and $^{232}ThF_4$ onto 30-μg/cm^2-thick Formvar backings. The backings were covered by 10–15 μg/cm^2 Au to make them electrically conducting. The average thickness of the fissile targets was about 130 and 70 μg/cm^2, respectively, for the thorium and uranium deposits. The target diameter was about 4 cm. The MFGIC sections 1–3 (in order of increasing distance from the Li target) were loaded with the thorium targets, while the uranium ones were placed into the sections 5–7. In the central (the fourth) section, a calibration ^{252}Cf source was mounted. It was prepared by self-sputtering onto a 50-μg/cm^2-thick Al_2O_3 backing covered by an Au layer with a thickness of about 15 μg/cm^2.

D. Data acquisition

The data acquisition system allows measurement of fragment-mass distributions for seven fissile targets simultaneously. Figure 3 shows a block diagram of the electronics used

to process the signals from the MFGIC. Each section of the detector operates as a twin Frisch-gridded ionization chamber (see Fig. 4). Three signals, two anode signals and a cathode signal, were taken from the chamber electrodes making use of low-noise charge-sensitive preamplifiers (PAs). Each anode's PA was placed in a common housing with a spectroscopy amplifier. The amplified and shaped anode signals were fed to peak-sensing analog-to-digital converters (ADCs) to determine the anode pulse heights, which are approximately proportional to the fragment energies (see Sec. III B). The timing outputs of anode PAs were fed to timing filter amplifiers (TFAs) with shaping constants $\tau_{\rm int} = 20$ ns, $\tau_{\rm dif} = 200$ ns and then to leading edge discriminators (LEDs). The logic signals from the LEDs were fed (as stop signals) to time-to-digital converters (TDCs) to measure the electron-drift times necessary to determine the fragment emission angles (as described in Sec. III C). To simplify the data acquisition system, alternate anodes were connected together, so only two spectroscopy channels instead of 14 were used to treat the anode signals from all sections. In principle, such a connection of the anodes can result in a pileup of the anode signals from different sections. However, the probability of coincidence events in different chambers was negligibly small at the counting rates ($\leqslant 10\ {\rm s}^{-1}$) encountered in the present experiment.

The cathode signal was used to measure the neutron energy by time of flight as well as to identify the chamber fired. The timing output of the cathode PA was fed to a TFA with shaping time constants $\tau_{\rm int} = \tau_{\rm dif} = 20$ ns. The output signal of the TFA was input to a constant fraction discriminator (CFD). Each of the seven CFDs delivers two output signals. One logic signal from the CFD entered an input register to identify the number of the chamber fired. The other signal was split into four branches to strobe an ADC and the input register as well as to form the start and stop signals necessary for measurement of the time interval between the fission event and the cyclotron radio freequency (rf). Data reading was started as soon as the "look-at-me" signal was generated by the TDC. For each event the data acquisition program read out the number of the chamber fired, two anode pulse heights, and three time intervals. The data were then stored event by event on a hard disk.

III. DATA ANALYSIS

A. Fragment-mass determination

A twin Frisch-gridded ionization chamber makes it possible to measure the fragment kinetic energies and cosine of the emission angle with respect to the normal on the cathode plane. Having the energies of the complementary fragments in the c.m. system, one can determine the fragment masses using the double kinetic energy ($2E$) method based on the conservation laws of mass and linear momentum. Ideally, the pre-neutron-emission fragment masses m_i^* ($i = 1, 2$) are calculated as

$$m_1^* = A_{\rm CN}\frac{E_2^*}{E_1^* + E_2^*}, \quad m_2^* = A_{\rm CN} - m_1^*, \tag{1}$$

where $A_{\rm CN}$ is the mass number of the compound nucleus and E_i^* the pre-neutron-emission fragment kinetic energies in the c.m. system. In practice, however, only post-neutron-emission fragment kinetic energies E_i can be measured. If we assume that the emission of neutrons by fission fragments is isotropic, E_i^* can be evaluated as

$$E_i^* = E_i\left(1 + \frac{\nu_i(m_i^*)}{m_i}\right), \tag{2}$$

where $\nu_i(m_i^*)$ is the average number of neutrons emitted from the fragment and m_i is the fragment mass after neutron emission:

$$m_i = m_i^* - \nu_i(m_i^*). \tag{3}$$

From Eqs. (1)–(3) the pre-neutron-emission fragment masses and energies were determined through an iterative procedure similar to that described in Ref. [19]. As the first step it was assumed that $m_1^* = m_2^* = (A_{\rm CN} - \nu_{\rm pre})/2$ where $\nu_{\rm pre}$ is the prefission neutron multiplicity taken from Ref. [20]. After this the new m_i^* were calculated through Eq. (3). Then the post-neutron-emission fragment energies were calculated as described in the subsequent subsection and the pre-neutron-emission kinetic energies were determined through Eq. (2) using the mass dependence of ν_i from Ref. [14]. After this the new m_i^* values were determined through Eq. (1) (with $A_{\rm CN} - \nu_{\rm pre}$ instead of $A_{\rm CN}$) and the calculation was repeated. The iteration process was stopped as soon as Δm_i^* was less than 1/10 amu.

The fragment-mass distributions obtained were further corrected for the wrap-around background as well as for the mass dispersion due to the prompt neutron emission and instrumental effects. These corrections are discussed in Secs. III D and III E, respectively.

B. Post-neutron-emission fragment kinetic energies

The post-neutron-emission fragment energy in the laboratory system was obtained from the anode pulse height $P_{\rm anode}$ as

$$E_i^{\rm lab} = A_\alpha P_{\rm anode} + \Delta_{\rm grid} + \Delta_{\rm PHD} + \Delta_{\rm loss}, \tag{4}$$

where A_α is a constant obtained from an absolute energy calibration using α particles from the ^{252}Cf source and a high-precision pulse generator, $\Delta_{\rm grid}$, $\Delta_{\rm PHD}$, and $\Delta_{\rm loss}$ are the corrections for the grid inefficiency, detector pulse-height defect (PHD), and fragment energy losses in the target material and backing, respectively.

The grid inefficiency correction is given in Ref. [21]:

$$\Delta_{\rm grid} = \frac{A_\alpha P_{\rm anode}\sigma_{\rm grid} R\cos\theta}{d}, \tag{5}$$

where $\sigma_{\rm grid}$ is the grid inefficiency, θ is the fragment emission angle with respect to the normal on the cathode plane, d is the cathode-to-grid distance, and R is the distance of the center of gravity of the ion-electron pair track from the origin of the track. The $\sigma_{\rm grid}$ value depends on the grid dimensions as well as on the cathode-anode distance. We used $\sigma_{\rm grid} = 0.040$ as given in Ref. [22]. To find R it was assumed that it depends on the fragment energy only. The energy dependence of R was found experimentally with the method proposed in Ref. [21]. The fragment emission angle determination is described in the next section.

The correction for the fragment energy losses was obtained as $\Delta_{\rm loss} = \Delta E_i^{\rm lab}/\cos\theta$, where $\Delta E_i^{\rm lab}$ is the average energy loss of the fission fragments in the layers traversed at $\theta = 0^\circ$. The $\Delta E_i^{\rm lab}$ values were calculated with the SRIM code [23].

The pulse-height defect was calculated as $\Delta_{\rm PHD} = a + bm_i$ with constants $a = 0.54$ MeV and $b = 0.034$ MeV/u obtained from the analysis of the PHD measurement in Ref. [24].

The post-neutron-emission fragment energy in the c.m. system was calculated through

$$E_i = E_i^{\rm lab} + \frac{p_F^2}{2A_F} - 2p_F\left(\frac{E_i^{\rm lab}}{2A_F}\right)^{1/2}\cos\theta, \qquad (6)$$

where p_F and $A_F = A_{\rm CN} - \nu_{\rm pre}$ are the average longitudinal linear momentum and mass of the fissioning nucleus, respectively. The linear momentum transfer (LMT) from the incident neutron to the fissioning nucleus was calculated with the systematics obtained for the (p,f) reactions in Ref. [25].

C. Fragment emission angle

Figure 4 illustrates how the fragment emission angle was measured. Both fission fragments are stopped in the space between cathode and grids, producing ion-electron pairs along their tracks. High voltage applied between the electrodes makes both free electrons and ions drift toward the anodes and cathode, respectively. Since the grid screens the anodes against the charge moving in the space between the cathode and grid, the anode pulse increase does not occur until the first electrons penetrate the grid.

By measuring the time difference T between cathode and anode signals one can determine the fragment emission angle by

$$\cos\theta = \frac{d-x}{r} = \frac{d - v_{\rm drift}T}{d - v_{\rm drift}T_{\rm min}}, \qquad (7)$$

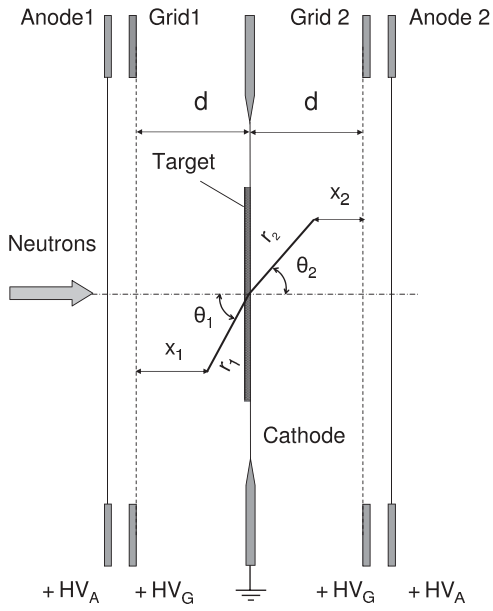

FIG. 4. Schematic drawing of a twin Frisch-gridded ionization chamber.

where r stands for the track length, x is the distance from the end of the track to the corresponding grid plane, $v_{\rm drift}$ is the electron drift velocity, and $T_{\rm min} = T\ (\cos\theta = 1)$. Substitution of $d = v_{\rm drift}T_{\rm max}$ by $T_{\rm max} = T\ (\cos\theta = 0)$ in Eq. (7) gives an expression for $\cos\theta$ that is more convenient for practical use:

$$\cos\theta = \frac{T_{\rm max} - T}{T_{\rm max} - T_{\rm min}}. \qquad (8)$$

The $T_{\rm min}$ and $T_{\rm max}$ values were determined experimentally. In the data analysis we used the approximation that the track length depends on the fragment energy only. In this case, the energy dependence of $T_{\rm min}$ can be found from the T distributions obtained with different cuts imposed on the fragment energy. The $T_{\rm max}$ values derived from these distributions are the same for all fragments.

D. Wrap-around background

The time-of-flight (TOF) technique was applied to identify those fission events induced by peak neutrons. In fact, a short proton beam micropulse spacing (55–72 ns) makes it possible to measure only time intervals between the fission events and the rf signals. As a result, the time distributions suffer from so-called wrap-around background caused by slow neutrons arriving at the detector simultaneously with fast neutrons from the next micropulse. Because of the wrap-around neutrons the resulting time distribution is a sum of the frame-overlapping distributions corresponding to different rf pulses. As a result, the high-energy peak is "seated" on top of a low-energy neutron background, and it is impossible to discriminate between them by just imposing a cut on the TOF interval. A proper subtraction of the wrap-around background can be done provided we know how many neutrons of given energy are under the high-energy peak and their energy, and use a model to calculate fission fragment-mass yields. For this purpose, the TOF distributions were simulated by a Monte Carlo folding of the neutron-induced fission cross sections of ^{232}Th [26] and ^{238}U [27] with the neutron spectra [17]. To fill the gap in the neutron spectra at low energies (see Fig. 2) we used a constant approximation. The cyclotron rf period, the detector time resolution, and the neutron flight path were taken into account to fit the experimental conditions.

An example of the time distribution simulated for the uranium fission induced by quasimonoenergetic neutrons with peak energy 32.8 MeV is given in Fig. 5(a) in comparison with the measured one. The frame-overlapping components of the simulated distribution are shown in Fig. 5(b). One can see that fission events induced by low-energy neutrons form a background under the high-energy peak. Such events comprise about 2.5% of the events at the high-energy peak (integrated over the full width at one-tenth of the maximum). The fraction of these events increases as the neutron energy increases to 3.0% and 4.0% for the neutron spectra with peak energies of 45.3 and 59.9 MeV, respectively. It is seen that the simulated time distribution reproduces rather well the experimental one. Since the frame-overlap structure of the time distributions was known, we were able to obtain the background mass distributions. For this purpose we used systematics for primary fragment mass yields [28] for $E_n \geqslant 5$ MeV

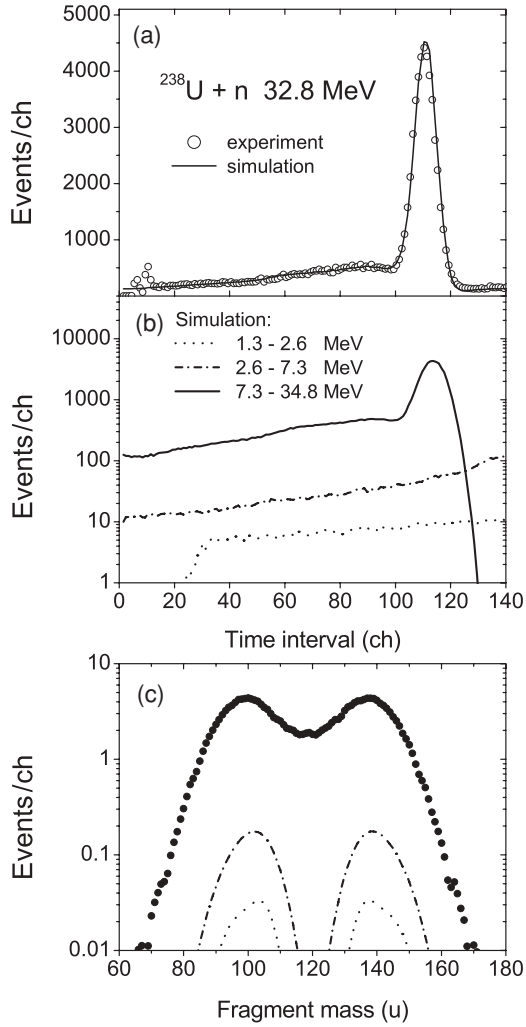

FIG. 5. (a) Simulated distribution of time intervals between the uranium fission events and the cyclotron rf signals (line) as compared to the measured one (symbols). (b) Components of the time distribution simulated for frame-overlapping rf periods. The channel width is 0.5 ns for both (a) and (b). (c) Primary fragment mass distribution obtained for all fission events under the high-energy peak (symbols) and the background distributions due to wrap-around neutrons with energies of about 2.2 MeV (dotted line) and 5.5 MeV (dash-dotted line) falling under the peak.

and the experimental data from Ref. [29] for $E_n < 5$ MeV. In Fig. 5(c) the calculated background mass distributions from the first and second rf periods are shown together with the pre-neutron-emission fragment-mass distribution measured for all fission events falling into the time interval within the high-energy peak. The mass resolution corrections were not taken into account at this stage.

E. Correction for the mass dispersion

The pre-neutron-emission fragment-mass distributions obtained as described above were then corrected for the mass resolution. The mass resolution function was calculated as in Ref. [30]:

$$\sigma^2_{\rm tot}(m) = \sigma^2_{\rm inh} + \sigma^2_{\rm inst}, \tag{9}$$

TABLE I. Fragment-mass resolution budget.

E_n (MeV)	$\sigma^2_{\rm FF}$	$\sigma^2_{\rm CN}$	$\sigma^2_{\rm LMT}$	$\sigma^2_{\rm det}$	$\sigma^2_{\rm tag}$	$\sigma^2_{\rm tot}$	FWHM
32.8	2.2	3.4	5.2	0.73	2.9	14.4	8.9
45.3	2.1	5.0	7.3	0.72	2.9	18.1	10.0
59.9	2.1	6.8	9.7	0.72	2.9	22.2	11.1

where $\sigma^2_{\rm inh}$ stands for the inherent broadening due to prompt neutron emission and $\sigma^2_{\rm inst}$ is the instrumental broadening caused by the measurement technique. The inherent mass dispersion can be written as

$$\sigma^2_{\rm inh}(m) = \sigma^2_{\rm FF} + \sigma^2_{\rm CN} + \sigma^2_{\rm LMT} \tag{10}$$

where $\sigma^2_{\rm FF}$ is the mass variation due to neutron emission from the fission fragments, $\sigma^2_{\rm CN}$ is the mass variation due to the prefission neutrons, and $\sigma^2_{\rm LMT}$ approximates the variance in mass caused by dispersion of the LMT distribution. Since we found that the mass dependence of $\sigma^2_{\rm tot}$ is small, the variances were calculated for the symmetric split only. The first term of Eq. (10) was calculated as in Ref. [30]:

$$\sigma^2_{\rm FF} = \frac{(A_{\rm CN} - \nu_{\rm pre})\nu_{\rm post}\overline{E_n}}{3\overline{E_K}} + \frac{1}{4}\sigma^2_{ff}(\nu_{\rm post}), \tag{11}$$

where $\overline{E_K}$ is the average of the total fragment kinetic energy (TKE), $\nu_{\rm pre}$ and $\nu_{\rm post}$ stand for the pre- and postscission neutron multiplicities, $\overline{E_n}$ denotes the average c.m. energy of the postscission neutrons, and σ^2_{ff} is the variance of the postscission neutron multiplicity. The TKE values were obtained in the present work. The multiplicities and the average neutron energy were estimated by interpolating between the experimental data obtained for proton-induced fission of ^{232}Th and ^{238}U at 27 and 63 MeV [31]. The $\sigma^2_{ff}(\nu_{\rm post})$ values as well as the second term of Eq. (10) were calculated for the ^{238}U(n,f) reaction as in Ref. [14]. The same values were applied to the case of ^{232}Th. The mass variance due to the LMT dispersion was estimated using Eq. (6) and the data on the LMT dispersion measured for the proton-induced fission of ^{238}U and taken from Ref. [32].

The instrumental mass dispersion for symmetric mass splitting was calculated as

$$\sigma^2_{\rm inst} = \sigma^2_{\rm det}\frac{(A_{\rm CN} - \nu_{\rm pre})^2}{2\overline{E_K^2}} + \sigma^2_{\rm tag}. \tag{12}$$

Here $\sigma^2_{\rm det} = 0.73$ MeV^2 is the variance in energy due to the detector resolution and $\sigma^2_{\rm tag}$ is the variance in mass resolution due to energy losses in the fissile deposit and backing. The measured mass TKE distributions (uncorrected for the mass resolution) and the fragment energy losses in the target and backing [23] were used in a Monte Carlo simulation of the fragment emission process in order to estimate the $\sigma^2_{\rm tag}$ values. The fragment-mass resolution budget is given in Table I.

With the estimated mass resolution, we found the final mass distribution through an iteration procedure implemented in the GRAVEL code [33]. An example of the unfolded mass distributions is given in Fig. 6 in comparison with the uncorrected ones.

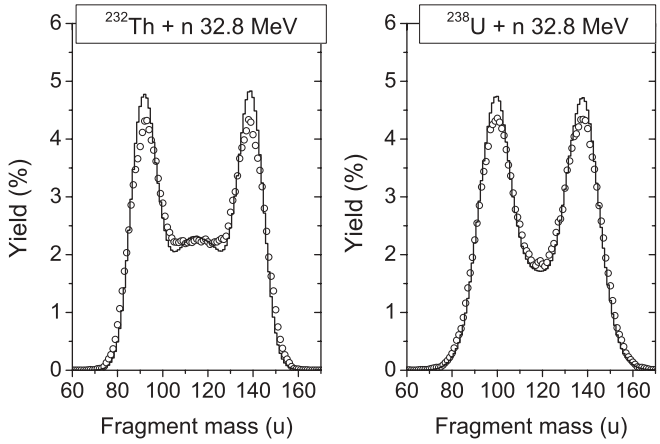

FIG. 6. Pre-neutron-emission fragment-mass distributions uncorrected (symbols) and corrected (lines) for the mass resolution for ^{232}Th (left) and ^{238}U (right) at a neutron energy of 32.8 MeV. The mass yields are normalized to 200%.

IV. MEASUREMENT RESULTS

Our experimental results are presented in Fig. 7. Note that the entire experiment took about two weeks at the proton beam current of about 10 μA. As mentioned above, the only measurement of mass yields in neutron-induced fission at intermediate energies was done at LANSCE for ^{238}U [14]. These data are also presented in Fig. 7. Notice that mass yields in Ref. [14] are given not for a single incident neutron energy, but for the incident energy intervals. For the energy range under comparison, the width of these intervals varies from 11 to 14 MeV. In our experiments, the uncertainty of incident neutron energy is mainly determined by the energy loss of protons in the lithium target, so it is $\pm$1.8, $\pm$1.5, and $\pm$1.2 MeV for the neutron peak energies 32.8, 45.3, and 59.9 MeV, respectively.

The mass yields in Ref. [14] were also obtained with the 2E method. However, fission fragments were detected in Ref. [14] at emission angles (with respect to the neutron beam axis) close to 90°, while our data were obtained at emission angles in the range 0°–60°.

V. THEORETICAL CALCULATIONS

A. Model of mass distribution

The formation of the fission fragment-mass distributions is mainly connected with properties of the potential energy surface at the stage of the saddle-to-scission descent. Our model treats the fission fragment formation as a result of the nuclear shape oscillations related to the mirror-asymmetry degree of freedom [7]. We consider these oscillations in the potential well formed by a collective nuclear potential which is determined by the macroscopic-microscopic method by

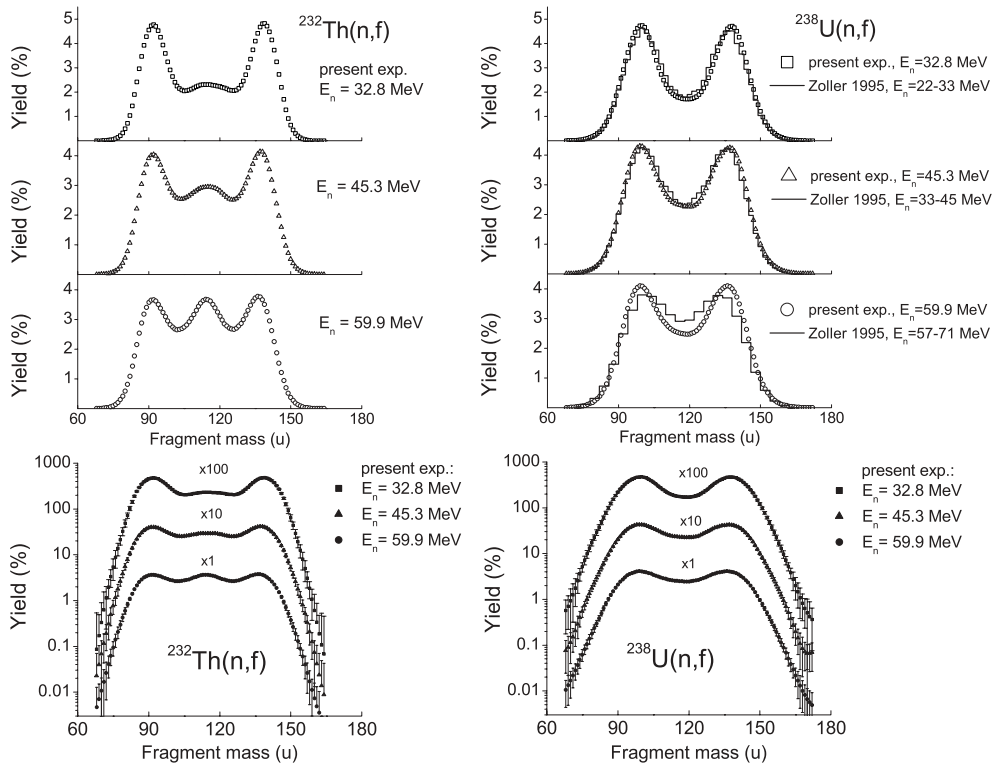

FIG. 7. Pre-neutron-emission fragment-mass distributions measured in neutron-induced fission of ^{232}Th (left column) and ^{238}U (right column) at 32.8 MeV (squares), 45.3 MeV (triangles), and 59.9 MeV (circles). Experimental data obtained at LANSCE for ^{238}U (Zöller *et al.* [14]) are given by solid histograms. For clarity of comparison, we do not show experimental uncertainties in the top panels. The mass yields are normalized to 200%. The bottom figure represents the logarithmic plot of the same data set shown as a linear plot on the top.

Strutinsky [34] in the one-center shape parametrization. A solution of the Schrödinger equation in such a potential gives us the fragment-mass spectra. The temperature dependence of fragment-mass yields is naturally determined in this model through the temperature dependence of the collective potential and the population of collective states in the potential well. The first effect results in a transition from asymmetric to symmetric fission while the second one accounts for a broadening of fragment-mass distributions with increasing nuclear temperature.

The choice of nuclear shape parametrization is an important point in studies of nuclear configurations near the scission point. We use the method proposed in Ref. [35] for axially symmetrical configurations. The nuclear shape is defined in the orthogonal coordinate system where the base family of coordinate surfaces consists of deformed Cassini ovaloids. This approach makes it possible to describe both oblate and prolate shapes, including the strongly prolate ones which are encountered in the latter stages of fission.

We consider three main parameters of deformation $\{\tilde{\alpha}\} = (\alpha, \alpha_1, \alpha_4)$, where α is the lemniscate parameter, α_1 defines the mirror symmetry of the nuclear shape, and α_4 is the parameter of the hexadecapole deformation. At small values of the lemniscate parameter the nuclear shape is an ovaloid while values $\alpha > 0.9$ correspond to configurations with a developed neck. The essential factor in our model is the dependence of the potential energy on α_1 near the scission point. The potential energy is calculated as

$$V_{\rm pot}\{\tilde{\alpha}\} = E_{\rm mac}\{\tilde{\alpha}\} + f(T)[\delta V\{\tilde{\alpha}\} + E_{\rm pair}\{\tilde{\alpha}\}], \qquad (13)$$

where $E_{\rm mac}$ is the smooth macroscopic potential energy part, δV is the shell correction, and $E_{\rm pair}$ is the pairing energy. The factor $f(T)$ in Eq. (13) accounts for the smearing of the shell-plus-pairing effects with increasing nuclear temperature T that results in a transition from asymmetric to symmetric fission at higher nuclear temperature. We take $f(T)$ in a Woods-Saxon form, $f(T) = 1 + \exp[(T - T_{\rm cr})/b])^{-1}$, where $T_{\rm cr} \approx 1.2$ MeV and $b \approx 0.15$ MeV are the model parameters.

We calculated the shell corrections and pairing energies (in the BCS approximation) separately for protons and neutrons using the standard procedures [36,37] developed in the frame of the independent-particle model. Single-particle spectra are calculated with the DIANA code [38]. The nuclear shape is taken in the lemniscate coordinate system. A deformed Woods-Saxon potential is used as a nuclear mean-field potential. Parameters of the potential and pairing interaction are chosen according to Ref. [39].

With increasing temperature, the collective potential is more and more defined by a smooth macroscopic part. We test three versions of macroscopic energy calculations: the liquid drop model with parameters from Ref. [40] and the finite-range models with the Yukawa [41,42] and the Yukawa-plus-exponential [43] potentials.

We assume that the fission fragment-mass distribution is formed near the scission point where the neck radius is about the radius of a nucleon (∼1 fm). It allows us to fix the lemniscate parameter value at $\alpha_{\rm sc} = 0.99$. By minimizing the potential energy at the scission point in the hexadecapole deformation α_4 we get the temperature-dependent potential energy as a one-dimensional function of α_1:

$$\widetilde{V}(\alpha_1) = V\left(\alpha_{\rm sc}, \alpha_1, \alpha_4^{\rm min}(\alpha_1)\right). \qquad (14)$$

The fragment-mass distributions are found then from the solution of the collective Schrödinger equation:

$$\left\{-\frac{\hbar^2}{2\sqrt{B_1}}\frac{d}{d\alpha_1}\frac{1}{\sqrt{B_1}}\frac{d}{d\alpha_1} + \tilde{V}(\alpha_1)\right\}\psi_\nu(\alpha_1) = E_\nu\psi_\nu(\alpha_1), \qquad (15)$$

where B_1 is the mass parameter related to α_1, and $\psi_\nu(\alpha_1)$ and E_ν are the collective wave functions and energies of the collective states, respectively. In all calculations, we use the same mass parameter, $B_1 = 0.054A^{5/3}$, obtained from the analysis of spontaneous fission half-lives [44]. The collective wave functions are expanded in a series of oscillator wave functions in cylindrical coordinates.

Assuming a Boltzmann-like occupation of the excited states, one can calculate the probability of finding the scission configuration with the mass asymmetry parameter α_1 as

$$Y(\alpha_1) \propto \sum_\nu |\psi_\nu(\alpha_1)|^2 e^{-E_\nu/T}. \qquad (16)$$

The fragment mass spectra are then calculated as follows:

$$Y(A_f(\alpha_1)) \propto Y(\alpha_1)\frac{dA_f}{d\alpha_1}, \qquad (17)$$

where the mass of a fragment A_f is related to α_1 through

$$A_f = 2\pi\frac{A}{V}\int_{z_{\rm min}}^{z_l}\rho^2(z)dz. \qquad (18)$$

Here A and V are the mass number and the volume of the fissioning nucleus, respectively, $\rho(z)$ is the surface equation in cylindrical coordinates, $z_{\rm min}$ is the z value at the minimum of the neck radius, and z_l is the z value at the nucleus edge. Note that A_f shows almost linear dependence on α_1 for the shape parametrization that we use in this work.

B. Multichance fission

Multichance fission (i.e., fission preceded by neutron evaporation) is possible if the excitation energy of the compound nucleus exceeds the sum of the fission barrier and the neutron binding energy. In this case, any fission observable, including the fission fragment-mass distribution, is a superposition of contributions from various fission chances. In addition, one should bear in mind that at $E_n \gtrsim 15$ MeV fission can be preceded not only by compound processes, but also by preequilibrium ones, including multiple preequilibrium emission. At the incident energies under consideration the resulting fragment-mass distribution reads as

$$Y(A_f) \propto \frac{1}{\sigma_f^{\rm tot}}\sum_i\int Y_i(A_f, E)\,\sigma_f^i(E)\,dE, \qquad (19)$$

where the summation index i runs over all atomic and mass numbers of fissioning nuclei as well as over their total angular momenta and parities, E denotes the excitation energy, and $\sigma_f^{\rm tot}$ is the sum of partial fission cross sections $\sigma_f^i(E)$ (per unit

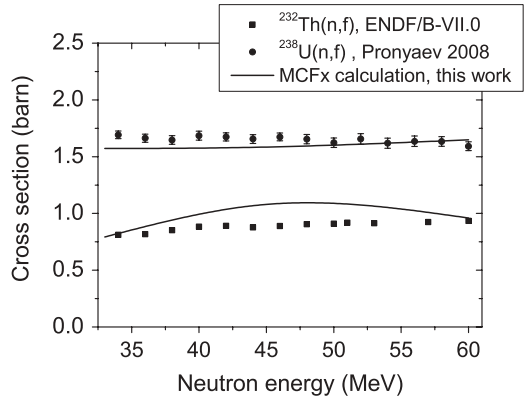

FIG. 8. Neutron-induced fission cross sections of ^{232}Th and ^{238}U calculated with the MCFX code in comparison with recent evaluations [26,27].

energy) taken over all the nuclei and nuclear states contributing to fission:

$$\sigma_f^{\text{tot}} = \sum_i \int \sigma_f^i(E)\, dE. \tag{20}$$

Thus, the calculation of partial fission cross sections is the problem to be solved if one wants to calculate the fission fragment-mass distributions at fairly high excitation energies. For this purpose, we use the MCFX code [9] combining advantages of the cascade and preequilibrium models with detailed Hauser-Feshbach statistical description of the final reaction stage. The neutron-induced fission cross sections of ^{232}Th and ^{238}U calculated with the MCFX code in the energy range 30–60 MeV are given in Fig. 8 in comparison with recent evaluations [26,27]. The model of fragment-mass distributions described in the previous subsection was implemented into the MCFX code to calculate the mass yields according to Eq. (19). The calculation results are compared with the experimental data in Fig. 9.

VI. DISCUSSION

As one can see from Fig. 9, our experimental data as well as the results of the model calculations demonstrate that the probability of symmetric fission increases with incident neutron energy for both ^{232}Th and ^{238}U. It is also seen that the symmetric fission is more enhanced for ^{232}Th than for ^{238}U. For the former target there are no other neutron data to compare with, but the experimental data available for the ^{238}U(n,f) reaction [14] as well as the data on proton-induced fission [31,45,46] show the same trends in the incident energy region under study.

When the present experimental data are compared with those from Ref. [14], one should keep in mind that in this work the incident neutron energy is more accurately defined than in Ref. [14]. In our work, the incident neutron energy is determined with a relative uncertainty of 2.0%–5.4%

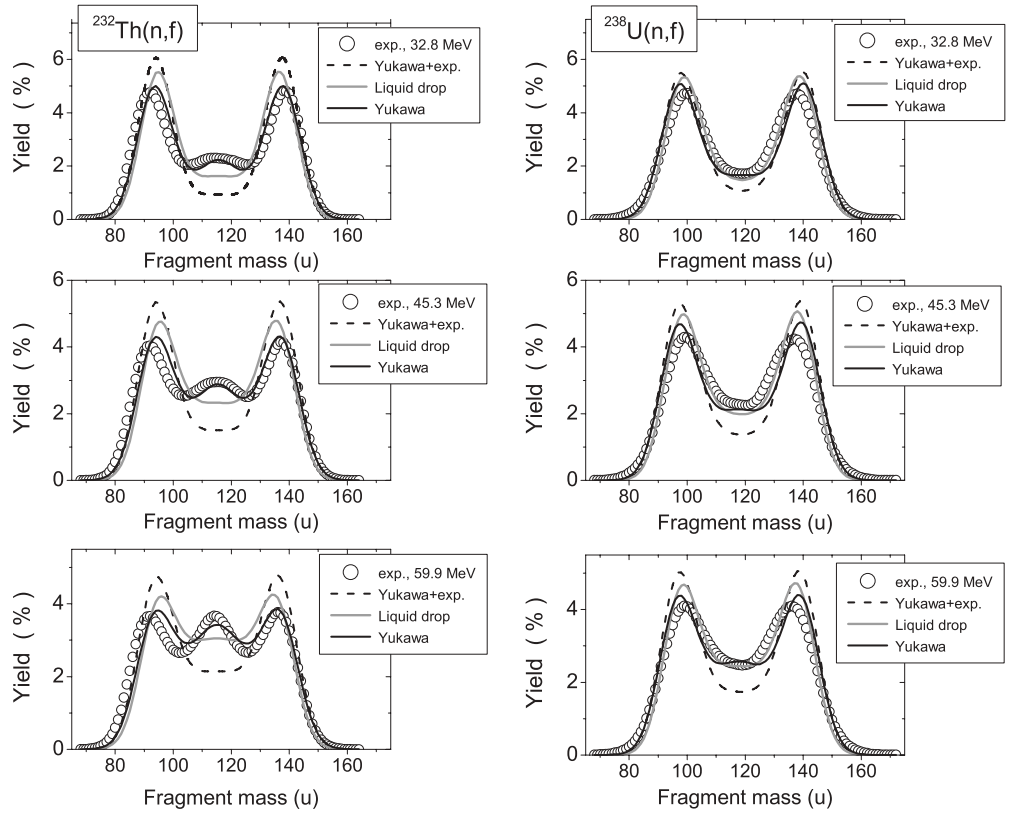

FIG. 9. Present experimental data (open circles) compared to the MCFX calculations for the neutron-induced fission of ^{232}Th (left column) and ^{238}U (right column). The calculation results are given for three versions of macroscopic energy calculations: the liquid drop model [40] (gray line) and the finite-range models with the Yukawa [41,42] (solid line) and the Yukawa-plus-exponential [43] potentials (dashed line).

depending on the neutron peak energy (see Sec. IV). For the measurements at the white neutron source the uncertainty of the incident neutron energy is mainly given by the width of the energy cut imposed. The incident neutron energies of interest are given in Ref. [14] with relative uncertainties of 10%–15% (see Fig. 7). Notice that our results at 32.8 and 45.3 MeV are compared with the data [14] taken at lower incident energies, so the agreement between the experimental results at these energies is worse than is seen from Fig. 7. As we mentioned in Sec. IV, the geometry of the present experiment differs from that used in Ref. [14]. We analyze fission fragments emitted in the solid angles around the neutron beam axis ($0.5 < |\cos\theta| < 1.0$), while the measurements [14] were done at 90° relative to the neutron beam. Experimental studies of mass-angular correlations in neutron- and proton-induced fission show that angular anisotropy of fission fragments increases with mass asymmetry [48–50]. Therefore we suppose that the difference between our data and the data in [14] can be to some extent attributed to mass-angular correlations.

It is seen from Fig. 9 that the model calculations agree qualitatively with the experimental results for both reactions. All three options for the macroscopic part of the potential energy allow us to reproduce the transition from asymmetric to symmetric fission with increasing incident neutron energy. We found it impossible to change the standard set of parameters proposed for the liquid drop [40] and the Yukawa-plus-exponential [43] potentials because these parameters are constrained by numerous fits to experimental data on nuclear masses, fission barriers, ground state deformations, heavy ion interaction potentials, etc. In this sense, the Yukawa potential [41] is less explored, so to fit the experimental data we keep all parameters suggested in Ref. [41] unchanged except the coefficient in the isotopic dependence. The calculation results given in Fig. 9 are obtained by using the coefficient 2.3 instead of 4 from Ref. [41]. One can see that this option makes it possible to describe the symmetric peak in the fission of ^{232}Th.

Finally, it is interesting to compare our experimental results with those available in nuclear data libraries. Note that data on pre-neutron-emission fragment-mass yields are not presented in the nuclear data libraries. Instead, we can use for comparison the library data on the mass-number yields which are the sum of all independent yields of a particular isobaric mass chain [51]. In the intermediate-energy domain, the existing experimental database for the fission yields suffers from significant data gaps and uncertainties. Recently, the energy-dependent fission product yields for actinide fission induced by neutrons and light charged particles with energies up to 150 MeV have been produced for the UKFY4.1 library [47] using the Wahl model implemented in the CYPF code [52]. Figure 10 shows our experimental data in comparison with the mass-number yields from the UKFY4.1 library. One can see that the contribution of symmetric fission is overestimated in Ref. [47] for all reactions and all incident neutron energies. The shift in the mass distributions is due to neutron evaporation from the fission fragments.

VII. CONCLUSION

In the present paper, we report experimental data on the fragment-mass yields of ^{238}U and ^{232}Th produced in

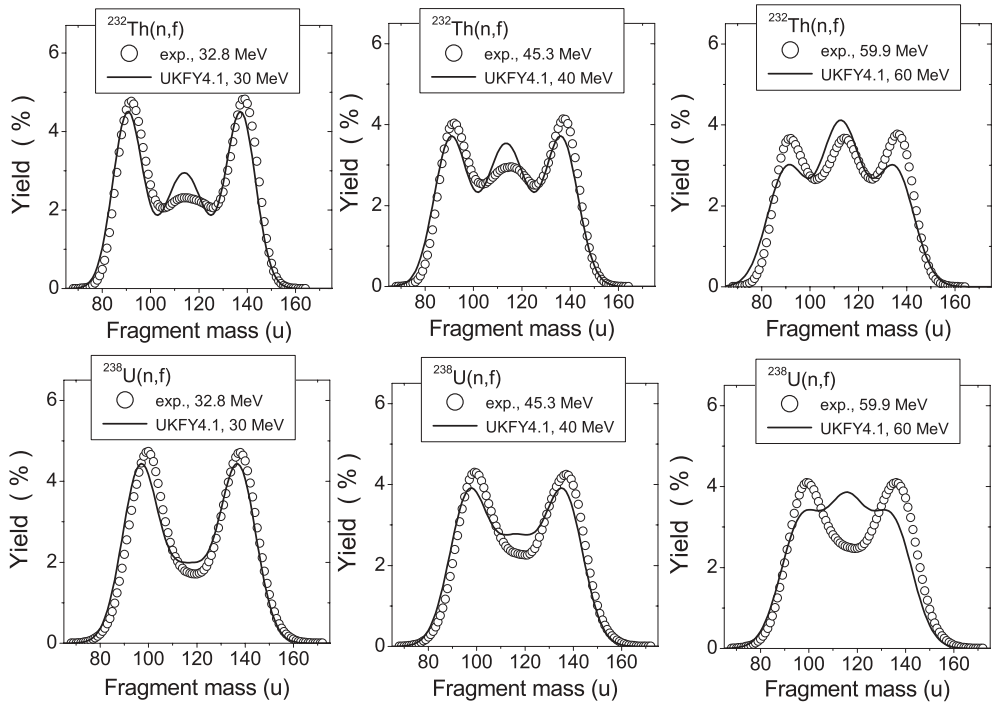

FIG. 10. Pre-neutron-emission fragment-mass distributions measured in the present work (symbols) in comparison with the mass-number yields from the UKFY4.1 library (lines) [47].

neutron-induced fission at the incident energies 32.8, 45.3, and 59.9 MeV. The experimental results demonstrate that the symmetric fission probability increases with incident neutron energy for both nuclides. However, symmetric fission is more enhanced in the case of ^{232}Th than in ^{238}U at the same incident neutron energies. The available data for ^{238}U [14], demonstrate the same trend but the symmetric fission contribution is higher in Ref. [14],as compared with the present data. In part, the difference between the two sets of experimental data may be explained by difference in the experimental geometry.

We also compared the experimental results with the model calculations carried out with the potential model of fission fragment formation [7] implemented in the nuclear reaction code MCFX [9]. Comparison with three types of potential energy calculations led us to conclude that the Yukawa potential model fits the experimental results best of all. However, to make a more definite conclusion, calculations of other fission observables are necessary in a wide range of fission reactions and incident energies.

It is worth mentioning that fragment-mass distributions calculated with the TALYS code [8] showed larger discrepancies with the experimental results than the present calculations. However, after implementation of a phenomenological model into the TALYS code, preliminary results show that rather good agreement can be achieved [53].

Compared to our experimental results, the UKFY4.1 data library [47] clearly overestimates the contribution of symmetric fission for ^{232}Th and ^{238}U at all incident neutron energies.

ACKNOWLEDGMENTS

The authors thank the operating crew of the Louvain-la-Neuve cyclotron facility for the excellent neutron beams they provided for these experiments. This work was supported in part by the International Science and Technology Center (Project No. 3192), the Swedish Radiation Safety Authority, the Swedish Nuclear Fuel and Waste Management Co, Ringhals AB within the NEXT project, and the European Commission within the Sixth Framework Programme through I3-EURONS (Contract No. RII3-CT-2004-506065).

[1] O. Hahn and F. Strassmann, Naturwissenschaften **27**, 11 (1939).
[2] I. Panov, E. Kolbe, B. Pfeiffer, T. Rauscher, K.-L. Kratz, and F.-K. Thielemann, Nucl. Phys. A **747**, 633 (2005).
[3] B. Wilkins, E. Steinberg, and R. Chasman, Phys. Rev. C **14**, 1832 (1976).
[4] J. Maruhn and W. Greiner, Phys. Rev. C **13**, 2404 (1975).
[5] M. C. Duijvestijn, A. J. Koning, and F.-J. Hambsch, Phys. Rev. C **64**, 014607 (2001).
[6] H. Goutte, J.-F. Berger, and D. Gogny, Int. J. Mod. Phys. E **15**, 292 (2006).
[7] S. Yavshits, in *Proceedings of the Second International Workshop on Compound Nuclear Reactions and Related Topics CNR*09, Bordeaux, 2009* [EPJ Web Conf. **2**, 08004 (2010)].
[8] A. Koning, S. Hilaire, and M. Dujvestijn, in *Proceedings of the International Conference on Nuclear Data for Science and Technology, Nice, 2007*, edited by O. Bersillon, F. Gunsing, E. Bauge, and R. Jacqmin (EDP Sciences, Les Ulis, France, 2008), p. 211.
[9] S. Yavshits, IAEA Report No. NDS-153, 2002, 2002 (unpublished); O. Grudzevich and S. Yavshits, in *Proceedings of the International Conference on Nuclear Data for Science and Technology, Nice, 2007* (Ref. [8]), Vol. 2, p. 1213.
[10] O. Shcherbakov *et al.*, in *Proceedings of the International Conference on Nuclear Data for Science and Technology, Tsukuba, 2001* [J. Nucl. Sci. Technol. Suppl. 2, **1**, 230 (2002)].
[11] A. Laptev, A. Donets, A. Fomichev, R. Haight, O. Shcherbakov, S. Solovyev, Y. Tuboltsev, and A. Vorobyev, in *International Conference on Nuclear Data for Science and Technology,* edited by R. Haight, M. Chadwick, T. Kawano, and P. Talou, AIP Conf. Proc. No. 769 (AIP, Melville, NY, 2005), p. 865.
[12] F. Tovesson and T. S. Hill, Phys. Rev. C **75**, 034610 (2007).
[13] F. Tovesson, T. S. Hill, M. Mocko, J. D. Baker, and C. A. McGrath, Phys. Rev. C **79**, 014613 (2009).
[14] C. Zöller, A. Gavron, J. Lestone, M. M. J. Theobald, A. Iljinov, and M. Mebel, IKDA Report No. 95/25, 1995(unpublished); C. Zöller, Ph.D. thesis, TH Darmstadt, 1995 (in German).
[15] A. Bol, P. Leleux, P. Lipnik, P. Macq, and A. Ninane, Nucl. Instrum. Methods Phys. Res. **214**, 169 (1983).
[16] C. Dupont, P. Leleux, P. Lipnik, P. Macq, and A. Ninane, Nucl. Instrum. Methods Phys. Res. A **256**, 197 (1987).
[17] H. Schuhmacher, C. Brede, V. Dangendorf, M. Kuhfuss, J. Meulders, W. Newhauser, and R. Nolte, Nucl. Instrum. Methods Phys. Res. A **421**, 284 (1999).
[18] I. Ryzhov *et al.*, Nucl. Instrum. Methods Phys. Res. A **562**, 439 (2006).
[19] F.-J. Hambsch, H.-H. Knitter, C. Budtz-Jørgensen, and J. Theobald, Nucl. Phys. A **491**, 56 (1989).
[20] V. Maslov, N. Kornilov, A. Kagalenko, and N. Tetereva, in *International Conference on Nuclear Data for Science and Technology* (Ref. [11]), p. 282.
[21] C. Budtz-Jørgensen, H.-H. Knitter, Ch. Straede, F.-J. Hambsch, and R. Vogt, Nucl. Instrum. Methods Phys. Res. A **258**, 209 (1987).
[22] O. Bunemann, T. Cranshaw, and J. Harvey, Can. J. Res. A **27**, 191 (1949).
[23] J. Ziegler, J. Biersack, and U. Littmark, *The Stopping and Range of Ions in Solids* (Pergamon Press, New York, 1985).
[24] F.-J. Hambsch, J. V. Aarle, and R. Vogt, Nucl. Instrum. Methods Phys. Res. A **361**, 257 (1995).
[25] A. Prokofiev and N. Olsson, Uppsala University Neutron Physics Report UU-NF 01#5 (2001).
[26] M. Chadwick *et al.*, Nucl. Data Sheets **107**, 2931 (2006).
[27] V. Pronyaev *et al.*, in *Proceedings of IAEA Co-ordinated Research Project on International Evaluation of Neutron Cross-Section Standards*, STI/PUB/1291 (IAEA, Vienna, 2008), p. 122.
[28] D. Gorodisskiy, K. Kovalchuk, S. Mulgin, A. Rusanov, and S. Zhdanov, Ann. Nucl. Energ. **35**, 238 (2008).
[29] F. Vivès, F.-J. Hambsch, H. Bax, and S. Oberstedt, Nucl. Phys. A **662**, 63 (2000).
[30] L. Glendenin, J. Unik, and H. Griffin, in *Proceedings of the First International Symposium on Physics and Chemistry of Fission, Salzburg, 1965* (IAEA, Vienna, 1965), p. 369.

[31] S. Isaev, R. Prieels, T. Keutgen, J. V. Mol, Y. E. Masri, and P. Demetriou, Nucl. Phys. A **809**, 1 (2008).
[32] M. Fatyga, K. Kwiatkowski, H. J. Karwowski, L. W. Woo, and V. E. Viola, Phys. Rev. C **32**, 1496 (1985).
[33] M. Matzke, Nucl. Instrum. Methods Phys. Res. A **476**, 230 (2002).
[34] V. Strutinsky, Nucl. Phys. A **122**, 1 (1968).
[35] V. Pashkevich, Nucl. Phys. A **169**, 275 (1969).
[36] V. Solovyev, *Theory of Complex Nuclei* (Nauka, Moscow, 1971).
[37] A. Bohr and B. Mottelson, *Nuclear Structure* (W. A. Benjamin, New York, 1974), Vol. 2.
[38] V. Rubchenya and V. Pashkevich, Bulletin, Petersburg Nuclear Physics Institute, 1976 (in Russian).
[39] V. Rubchenya and S. Yavshits, Yad. Fiz. **40**, 649 (1984); [Sov. J. Nucl. Phys. **40**, 416 (1984)].
[40] P. Seeger and W. Howard, At. Data Nucl. Data Tables **17**, 428 (1976).
[41] H. Krappe and J. Nix, in *Proceedings of the Third International Symposium on Physics and Chemistry of Fission, Rochester, 1973* (IAEA, Vienna, 1974), Vol. 1, p. 159.
[42] A. Dobrowolski, K. Pomorski, and J. Bartel, Phys. Rev. C **75**, 024613 (2007); Phys. Scr., T **125**, 188 (2006).
[43] H. J. Krappe, J. R. Nix, and A. J. Sierk, Phys. Rev. C **20**, 992 (1979).
[44] A. Sobiczewski, Fiz. Elem. Chastits. At. Yadra **10**, 1170 (1979) [Sov. J. Part. Nucl. **10**, 466 (1979)].
[45] V. Rubchenya *et al.*, Nucl. Instrum. Methods Phys. Res. A **463**, 653 (2001).
[46] O. Batenkov, V. Eismont, M. Majorov, A. Smirnov, K. Aleklett, W. Loveland, J. Blomgren, H. Condé, M. Duijvestijn, and A. Koning, in *International Conference on Nuclear Data for Science and Technology* (Ref. [11]), p. 625.
[47] R. Mills, JEF/DOC-1232 and UKNSF, 2008, P227.
[48] F. Gönnenwein and E. Pfeiffer, Z. Phys **207**, 209 (1967).
[49] B. Cohen, W. Jones, G. McCormick, and B. Ferrel, Phys. Rev. **94**, 625 (1954).
[50] H. Kudo, Y. Nagame, H. Nakahara, K. Miyano, and I. Kohno, Phys. Rev. C **25**, 909 (1982).
[51] A. Wahl, in *Proceedings of Specialists Meeting on Fission Product Nuclear Data*, Tokai, Japan, 1992, [Report NEA/NSC/DOC(92)9, p. 334].
[52] A. Wahl, Los Alamos Report No. LA-13928, 2002 (unpublished).
[53] V. Simutkin, M. Onegin, I. Ryzhov, and S. Pomp, in *Proceedings of the International Nuclear Physics Conference, Vancouver, 2010* (to be published).